Volume 13
Number 21
7 June 2025
Pages 15281–16252

Journal of Materials Chemistry A

Materials for energy and sustainability

rsc.li/materials-a

ISSN 2050-7488

ROYAL SOCIETY OF CHEMISTRY

PAPER
Markus Niederberger *et al.*
Shaping nanoparticle-based aerogels for efficient light-driven catalysis

Journal of
Materials Chemistry A

PAPER

View Article Online
View Journal | View Issue

Cite this: *J. Mater. Chem. A*, 2025, **13**, 15592

Shaping nanoparticle-based aerogels for efficient light-driven catalysis†

Fabian Matter,‡ David Kiwic,‡ Marco Bernet, Elena Tervoort and Markus Niederberger *

Received 19th December 2024
Accepted 3rd March 2025

DOI: 10.1039/d4ta09013f

rsc.li/materials-a

Aerogels synthesized from preformed metal oxide nanoparticles exhibit high crystallinity and can be manufactured in transparent form, making them appealing for photo- and photothermal catalysis. To date, translucent nanoparticle-based aerogels are primarily produced in monolithic form by casting techniques, which are labor-intensive and costly, and these centimeter-sized bodies are prone to mass transport limitations when applied in catalysis. Here, we present a simple process to prepare millimeter-sized worm-shaped and spherical aerogel granules with high optical clarity and large specific surface areas ranging from 130 to 550 $m^2\ g^{-1}$, using colloidally stable dispersions of TiO_2, ZrO_2, and In_2O_3 nanocrystals. These granules are easier to produce and handle, and our Pd/TiO_2 aerogel granules demonstrate superior photocatalytic performance in methanol decomposition, achieving nearly complete conversion of 1 mol% methanol in air at high flow rates (space velocity of ~115 $L\ g^{-1}\ h^{-1}$). This significant improvement over their monolithic counterparts highlights the potential of aerogel shaping to enhance their viability for practical applications such as the photocatalytic oxidation of volatile organic compounds.

1. Introduction

Photocatalysis provides promising solutions to pressing energy and environmental problems.[1] It enables the conversion of CO_2 into solar fuels,[2] the purification of water from toxic chemicals[3] or pesticides[4] and the depolymerization and upcycling of microplastics.[5] An important parameter in photocatalysis is the surface area of the catalysts, which is why nanopowders with their large surface area are particularly advantageous. Consequently, nanoparticles have become widely used in photocatalysis,[6] and decades of research have optimized their performance by fine-tuning composition, crystal structures, surface chemistry, and particle morphology.[7,8] While these strategies effectively refine the catalyst properties at the nanometer scale, they often overlook macroscopic factors. Properties such as light penetration depth and reactant transport through the bulk photocatalytic material profoundly influence catalytic efficiencies. Therefore, the macroscopic structure should also be taken into account when optimizing the photoactivity of a material.[9,10]

When designing photocatalysts for gas-phase applications, an effective strategy for preserving the high surface area of nanoparticles is to assemble them into aerogels.[11–13] By carefully selecting the nanoparticles and controlling the gelation process, it is possible to precisely tailor the composition and porosity of aerogels, which in turn affect their chemical and optical properties.[9] However, in photocatalytic applications, monolithic aerogels often encounter mass and light transport limitations due to the mesoporous structure and light scattering within the aerogel framework.[9,14] One approach to address these limitations is to modify the aerogel geometry by incorporating a 3D-printed scaffold, which improves both gas flow and ultraviolet light penetration.[15] While scaffold integration presents intriguing possibilities, it remains costly and difficult to scale. A more practical solution would be to shape the aerogel directly during production, enabling rapid mass transport, optimal illumination, and compatibility with a range of photoreactor designs.

Among various photocatalytically active materials that can be structured into aerogels, titanium dioxide (TiO_2) stands out due to its strong oxidation potential under ultraviolet light, making it highly promising for the decomposition of organic molecules.[16] Methanol is commonly studied as a model volatile organic compound (VOC) because of its extensive use in today's chemical industry and its projected role in a future methanol-based economy.[17] The photocatalytic activity of TiO_2 can be

---

Laboratory for Multifunctional Materials, Department of Materials, ETH Zurich, Vladimir-Prelog-Weg 5, 8093 Zurich, Switzerland. E-mail: markus.niederberger@mat.ethz.ch

† Electronic supplementary information (ESI) available: The experimental setup for the photocatalytic measurements; results of the X-ray fluorescence analysis; scanning transmission electron microscopy images of Pd/TiO_2 aerogels; photocatalytic performance of Pd/TiO_2 worm-shaped granules using different light sources; calculation of the apparent quantum efficiency. See DOI: **https://doi.org/10.1039/d4ta09013f**

‡ These authors contributed equally to this work.

further enhanced by combining it with metal nanoparticles.[18–20] Palladium (Pd), for instance, is highly effective in photocatalytic methanol reforming when paired with TiO_2.[21,22] Pd not only improves charge carrier separation, extending the lifetime of photoexcited electrons in TiO_2, but also provides active sites for the binding and dissociation of reactants and intermediates, resulting in superior photocatalytic performance.[23] Given the attractive properties of TiO_2 nanoparticles and the ease with which they can be combined with other nanoparticles, it is not surprising that TiO_2 nanoparticle-based aerogels have garnered substantial interest for photocatalytic applications. Aerogels combine high light transmittance with a large surface area (up to 550 m^2 g^{-1}), which is fully accessible due to their open porous microstructure. With a highly crystalline, photoactive matrix, TiO_2 aerogels meet key requirements for efficient gas-phase photocatalysis. For instance, large cylindrical monoliths of Au/TiO_2 aerogels have been studied for CO_2 reduction to methanol.[24] By optimizing the noble metal cocatalyst, these aerogels produced hydrogen efficiently from methanol and water vapor, generating 3.5 times more hydrogen compared to their powdered counterparts.[18] Further improvements were achieved through nitrogen doping of TiO_2, optimization of the palladium cocatalyst, and adjustments to the monolith's surface-to-volume ratio to enhance illumination.[25,26] These studies have highlighted the critical role of the macroscopic shape of aerogels in optimizing mass transport and catalyst illumination.[15,27] Notably, the penetration depth of 375 nm UV light into titania aerogels was found to be approximately 2–2.5 mm,[14,15] and mass transport within the aerogel network occurs primarily *via* Knudsen diffusion, resulting in relatively low permeability despite the material's high porosity.[9] Although reducing aerogel density can slightly improve transport rates, the adjustment range is very limited. As a result, aerogels with cross-sections larger than a few millimeters should be avoided to ensure complete catalyst illumination and minimize the length of diffusion pathways. Similar diameters are often employed in industrial catalysts to optimize mass transport.[28] Moreover, smaller aerogel shapes are easier to handle compared to fragile macroscopic monoliths. Spherical aerogels, with millimeter-sized diameters, have already been successfully produced using sol–gel methods.[29–31] For instance, Thoni *et al.* demonstrated the continuous production of Au/Al_2O_3 aerogel spheres using a heated droplet reactor.[29] While these developments are promising, achieving a narrower size distribution could further improve catalyst bed packing reliability and reduce pressure drops in industrial applications. Additionally, the sol–gel methods used in previous studies often result in metal oxide phases with poor crystallinity, limiting quantum efficiency and reducing photocatalytic activity.[32] Therefore, establishing a method to shape crystalline, nanoparticle-based gels into granular aerogels is crucial for maximizing photocatalytic efficiency and improving conversion rates.

Ideally, aerogel photocatalysts could even replace the more widely applied thermal catalysts in industry, particularly in applications such as the removal of odorous or hazardous volatile organic compounds (VOCs) from industrial emission streams. This process is crucial for industries aiming to reduce emissions, improve air quality, and comply with environmental regulations.[21,22] A variety of methods exist for mitigating VOC emissions, including adsorption on activated carbon filters, direct flaring, and catalytic decomposition.[33] Among these methods, thermal catalysis is the most versatile for handling fluctuating VOC concentrations. However it often requires high temperatures (250–500 °C), leading to significant energy consumption and operational costs.[21] In contrast, photocatalysis presents a promising alternative that could reduce these energy demands, provided that suitable photo- and photothermal catalysts are developed.

In this study, we present a straightforward and efficient method for preparing worm-shaped and spherical TiO_2 aerogel granules, both of which are ideal for photocatalysis. This method is also successfully adapted to ZrO_2 and In_2O_3, two other materials relevant for catalysts, which, to our knowledge, have not been produced as transparent nanoparticle-based aerogels. We characterize these aerogels using X-ray diffraction (XRD), scanning electron microscopy (SEM), gas sorption measurements, and thermogravimetric analysis (TGA) and compare their properties to those of the established monolithic aerogels. To evaluate the photocatalytic performance of the aerogel granules, we chose methanol oxidation in air, given its simplicity and relevance for VOC emissions mitigation. For this purpose, we fabricate worm-shaped and monolithic Pd/TiO_2 aerogels and test them under various illumination conditions and reactant flow rates in a custom-built photocatalytic reactor.

2. Experimental section

Chemicals & materials

Titanium(IV) tetrachloride (99.9% trace metal basis), indium(III) acetate (99.99% trace metal basis), palladium(II) acetate (≥99.9% trace metals basis), benzyl alcohol (puriss., 99–100.5% (GC)), tris-(hydroxymethyl)-aminomethane (Trizma base, puriss., ≥99.7%), hydrochloric acid (37%, for analysis EMSURE®), ethanol (absolute ≥ 99.8% for analysis), diethyl ether (puriss., ≥99.8%), *n*-hexane (≥97.0% for HPLC), and acetone (≥99.8% for HPLC) were purchased from Sigma-Aldrich/Merck. Zirconium(IV) tetrachloride (99.5%+, metal basis) was purchased from Alfa Aesar. Methanol (99.8% extra dry over MS) and 1,4-dioxane (≥99.8%, stabilized) were received from Fisher Scientific. Synthetic air (80/20 mol% N_2/O_2) was purchased from PanGas AG Switzerland. Silicone oil (Bluesil FLD 47 V350, Elkem) was purchased from Silitech AG Switzerland. All chemicals were used as received.

Synthesis of TiO_2 nanoparticles

Trizma-functionalized TiO_2 (anatase) nanoparticles were synthesized according to a previously published protocol.[9] Briefly, $TiCl_4$ (8 mL, 73 mmol) was added dropwise to ice-cooled ethanol (24 mL, 441 mmol) under constant stirring. Meanwhile, benzyl alcohol (160 mL) was preheated to 120 °C in an oil bath before Trizma (728 mg, 6 mmol) was added and dissolved over 1 min. The ethanolic precursor solution was then added to the preheated benzyl alcohol before the reaction vessel was closed with a perforated lid and kept for 2 h at 120 °C under constant stirring. After quenching the reaction by cooling to room temperature in a water bath, 24 mL aliquots of the reaction solution were mixed with diethyl ether (25 mL) to precipitate the particles. The white powder was collected by centrifugation (5 min, 4000 rpm) and washed three times with diethyl ether (3 × 40 mL) and hexane (3 × 40 mL). For each step, the wet precipitate was mixed with fresh solvent, shaken vigorously, and centrifuged for 1 min at 4000 rpm before the clear supernatant was discarded. Finally, the precipitate was suspended in hexane (30 mL) before water (4 mL) was added to extract the nanoparticles. After slight shaking and centrifugation (1 min, 4000 rpm) to improve phase separation, the clear aqueous dispersion (~220 mg mL^{-1}) was separated from the clear hexane phase with a syringe. All the colloidal dispersions of a batch were combined and stored overnight in a closed vial at room temperature before being diluted with water (1 : 1 vol/vol) and used for gelation.

Pd/TiO_2 dispersions were prepared analogously with an additional post-synthetic step. After synthesis of the TiO_2 nanoparticles at 120 °C for 2 h, a quarter of the reaction solution (47 mL) was transferred into a 100 mL round-bottom flask preheated to 140 °C. A solution of palladium(II) acetate (30.7 mg, 0.137 mmol) in benzyl alcohol (5 mL) was added, and the mixture was left for 15 min at 140 °C under constant stirring. During this time, the color changed from white to grey, indicating the formation of Pd nanoparticles. Washing and redispersion were performed as described above to obtain a dark brown colloidal dispersion.

Synthesis of ZrO_2 nanoparticles

ZrO_2 nanoparticles were synthesized in benzyl alcohol starting from zirconium(IV) chloride as a precursor. First, $ZrCl_4$ (2.91 g, 12.5 mmol) was added to ethanol (3 mL, 51 mmol) under constant stirring, forming a white solid under the release of hydrochloric acid. The mixture was stirred for another 10 minutes to allow for complete dissolution, yielding a colorless transparent solution. The ethanolic precursor solution was then transferred to a round-bottom flask filled with benzyl alcohol (150 mL) preheated in an oil bath to 200 °C. The reaction solution was kept at 200 °C for 30 min open to air, during which the initial colorless solution gradually turned milky. To increase the dispersibility for later processing, 4.5 mL of hydrochloric acid was carefully added to the hot reaction mixture. Upon addition, the formerly milky dispersion turned transparent under vigorous boiling. Right after addition, the mixture was removed from the oil bath and cooled to room temperature in a water bath. 24 mL aliquots of the reaction solution were mixed with a hexane–diethyl ether mixture (20 mL, 10 : 1 vol/vol) to precipitate the particles. The white precipitate was collected by centrifugation (4000 rpm, 5 min) and washed three times with diethyl ether (3 × 30 mL) and hexane (3 × 30 mL). The particles were finally extracted with water (15 mL) as described above. To allow further processing into gels, the aqueous dispersion was purified by centrifugal filtration (Amicon Ultra-15, 10 kDa MWCO). To this end, the initial dispersion was reduced from 15 mL to 3 mL, followed by dilution to 15 mL with deionized water. This washing step was performed 3 times in total. Subsequently, the concentrated viscous dispersions of the batch were combined and diluted to 9 mL to obtain the final ZrO_2 dispersion (~173 mg mL^{-1}).

Synthesis of In_2O_3 nanoparticles

In_2O_3 nanoparticles were synthesized by reacting indium(III) acetate with benzyl alcohol. First, benzyl alcohol (50 mL) was heated in a 100 mL round-bottom flask to 210 °C in an oil bath before indium acetate (5000 mg, 17.1 mmol) was added. The mixture was kept for 20 min at 210 °C open to air, during which time the solution changed from white (undissolved precursor suspension) to clear transparent (colloidally stable dispersion of nanoparticles). The reaction was finally quenched by cooling to room temperature in a water bath. The solution was passed through a syringe filter (PTFE, 0.45 μm) to remove traces of solid residues resulting from impurities of the precursor. For washing, 12 mL aliquots of the reaction solution were mixed with a hexane–diethyl ether mixture (30 mL, 9 : 1 vol/vol) to precipitate the particles. The white precipitate was collected by centrifugation (4000 rpm, 3 min) and washed three times with acetone (3 × 30 mL) as described above. The wet precipitate of an aliquot was redispersed in water (2 mL) to give ~2.4 mL of a clear, slightly yellowish colloidal dispersion (~240 mg mL^{-1}). Freshly prepared dispersions were used for gelation within the first hours due to the limited stability of the concentrated dispersion.

Gel and aerogel fabrication

Gelation of the aqueous dispersions was induced by the addition of nonsolvents and subsequent heating to 25–55 °C.[9,34,35] Depending on the system and desired geometry, different gelation conditions and solvent ratios were used (see Table 1). For monolithic samples, the dispersion was first destabilized by nonsolvent addition before being transferred into cut-open syringes. This mold was sealed with parafilm to prevent solvent evaporation during gelation. Once fully gelled, the monolithic gels were demolded into the corresponding solvent bath. For the preparation of granules and spheres, the destabilized dispersion was gelled in a syringe (typically 3 mL) sealed with a syringe cap. Shorter gelation times were applied compared to the monoliths to prevent the gel from becoming too rigid. Worm-shaped granules were produced by extruding the pre-gelled dispersion through a nozzle (1 mL micropipette tip, inner diameter ~ 800 μm) directly into a solvent bath, using a syringe pump at a rate of 2 mL min^{-1}. For spherical granules, the solvent bath was topped with a layer of silicone oil, and the pre-gelled dispersion was added dropwise through a needle (0.5 × 40 mm). Dioxane was chosen over acetone as a nonsolvent due to its higher density. This choice allowed the spherical gel beads to pass through the less dense silicone oil layer and then through the phase boundary into the denser dioxane–water layer, where they retained their spherical shape imparted by the hydrophobic oil layer. To ensure rapid gelation

Table 1 Gelation conditions used for the preparation of aerogel monoliths and worm-shaped and spherical granules. The initial concentration refers to the nanoparticle concentration before mixing; the nonsolvent concentration refers to the concentration after mixing, *i.e.*, 50% corresponds to a 1 : 1 ratio of dispersion and nonsolvent. Note that in practice the conditions can vary slightly since the stability of the aqueous nanoparticle dispersions can slightly change during storage

Material	Initial conc. [mg mL^{-1}]	Shape	Nonsolvent [vol%]	Gelation temp.	Gelation time	Bath (vol%)	Bath temp.
TiO_2	110	Monolith	Acetone (50%)	25 °C	60 min	Acetone (70%)	25 °C
		Worms	Acetone (50%)	25 °C	15 min	Acetone (70%)	25 °C
		Spheres	Dioxane (50%)	25 °C	5 min	Dioxane (80%)	55 °C
In_2O_3	240	Monolith	Acetone (66%)	55 °C	60 min	Acetone (90%)	25 °C
		Worms	Acetone (66%)	55 °C	30 min	Acetone (90%)	25 °C
		Spheres	Dioxane (60%)	55 °C	15 min	Dioxane (90%)	55 °C
ZrO_2	173	Monolith	Dioxane (55%)	55 °C	20 min	Acetone (75%)	25 °C
		Worms	Acetone (55%)	55 °C	30 min	Acetone (85%)	25 °C
		Spheres	Dioxane (55%)	55 °C	5 min	Dioxane (80%)	55 °C

of the spheres within the oil layer, the two-layer solvent bath was maintained at 55 °C.

The gels of all three geometries were aged in the corresponding bath at 55 °C overnight to reduce shrinkage during solvent exchange. In the case of the monolithic and worm-shaped samples, the aqueous pore fluid was gradually replaced by acetone (10% steps every 2 h). The spheres were collected from the dioxane–water phase and washed three times with pure dioxane to remove any potential oil contaminations, before the dioxane was replaced by repeated washing with pure acetone. After solvent exchange, the pore liquid was removed by supercritical drying with CO_2 (E3100, Quorum Technologies) at 42 °C and 100 bar as described in detail elsewhere.[9]

Characterization

X-ray diffraction (XRD) patterns were recorded on a Malvern PANalytical Empyrean diffractometer (PIXcel 1D detector, Cu K_α radiation, reflection mode, Si wafer). Thermogravimetric analysis (TGA) was performed on a Mettler Toledo TGA/DSC 3+ STARe instrument (Mettler-Toledo) using a heating rate of 10 °C min^{-1} under an ambient atmosphere. Nitrogen sorption data were collected on a Quantachrome Autosorb iQ at 77 K. Specific surface area and pore size distribution were determined using density functional theory (DFT) and a nonlocal density functional theory (NLDFT) equilibrium model for silica with cylindrical pores. Prior to analysis, samples of 20–70 mg were degassed at 100 °C for 24 h. The theoretical surface area of the individual nanoparticles was calculated from the bulk density and the corresponding crystallite size using simple geometric considerations (TiO_2 anatase: 3.88 g cm^{-3},[36] 3.1 nm; t-ZrO_2: 6.09 g cm^{-3},[37] 2.9 nm; c-In_2O_3: 7.04 g cm^{-3},[38] 6.8 nm). Optical microscopy images were recorded on a Keyence microscope (VHX-6000). Scanning electron microscopy (SEM) images were recorded on a Zeiss Gemini 2 instrument operated at 5 kV using an inlens detector. Small aerogel pieces were placed on conductive carbon tape and sputtered with 4 nm of Pt by a Safematic sputter coater CCU-010. The Pd/TiO_2 aerogels were further characterized using scanning transmission electron microscopy (STEM) with an FEI Talos F200X operating at 200 kV. For STEM imaging, a high-angle annular dark field (HAADF) detector was employed. High-resolution energy dispersive spectroscopy (EDS) was performed using a SuperX integrated EDS system equipped with four silicon drift detectors (SDDs). The Pd content in the photocatalyst was determined using X-ray fluorescence (XRF) spectroscopy on a Rigaku ZSX Primus IV spectrometer equipped with a 4 kW Rh source and analyzing crystal detectors, including LiF(200), Ge, PET, and RX26.

Photocatalytic measurements

The photocatalytic decomposition of methanol over Pd/TiO_2 aerogels was studied in a custom-built setup consisting of a gas preparation system, a continuous flow reactor,[14] and a gas chromatograph (see Fig. S1 in the ESI†). All samples used for these experiments were prepared from the same dispersion and supercritically dried under identical conditions. Before the tests, the samples were heat-treated at 350 °C for 20 h in air to increase the mechanical stability and prevent possible crack formation during photocatalytic testing. The monolithic sample (39 mg) was placed on a fine-meshed stainless steel grid (SD 265/50, Bopp Switzerland) attached to the bottom of a hollow cylinder made of PMMA (poly(methyl methacrylate)) discs with an inner diameter matching the monolith dimensions (see Fig. S1†). Granules (39 mg) were confined within the same cylindrical space to ensure equal photon flux across both samples. The mounted samples were first pretreated under a constant synthetic air stream of 20 sccm (standard cubic centimeters per minute) for 2 h under UV LED light (Thorlabs, M365LP1, λ: 365 nm, 2000 mW cm^{-2}) to remove any organic residues and exclude artifacts arising from shrinking under high irradiance. During the photocatalytic experiments, the samples were irradiated from both sides with UV LEDs ($\lambda = 365$ nm) equipped with aspheric condenser lenses. For a comparative study with visible light, two white light-emitting LEDs (Thorlabs, MCWHLP1, 400–800 nm) were used instead. The irradiance was calibrated using a thermal power sensor (Thorlabs S405C) and regulated during measurement *via* a computer-controlled setup (pulse width modulation, 100 Hz, 2000 mW cm^{-2}). The synthetic air flow was regulated using mass flow controllers (Alicat Scientific). To introduce methanol (MeOH) vapor into the gas stream, the headspace of a boiling MeOH solution was first passed through a reflux condenser set at 3 °C. This MeOH-enriched stream was then mixed with the dry synthetic air stream in different ratios (see Fig. S1 in the ESI†). During the experiments, the methanol concentration was adjusted between 0.05 and 1.00 mol%, the overall gas flow rate ranged from 20 to 75 sccm and the irradiance measured at the sample was varied between 0 and 1000 mW cm^{-2}. Each condition was maintained for at least 60 min for each measurement point. The outlet gas flow was monitored using a calibrated gas chromatograph (Micro GC Fusion, Inficon) equipped with three modules (Rt-Molsieve 5A with an Rt-Q-Bond Backflush, Rt-Q-Bond, and Rt-U-Bond) and a TCD detector. The reactor and gas chromatograph were connected through a heated line (80 °C). The outlet stream was sampled every 5 min.

3. Results & discussion

Preparation of monolithic, worm-shaped and spherical aerogels

The preparation of nanoparticle-based aerogels is based on the controlled destabilization of concentrated colloidal dispersions.[12,39] The stability (*i.e.*, the degree of agglomeration of the nanocrystals) of these dispersions has a major influence on the quality of the aerogels, particularly their optical transparency, mechanical stability and porosity. To produce nanoparticle-based aerogels from a specific material, it is important that the corresponding nanoparticles can be processed into stable colloidal dispersions. In addition to the titania (TiO_2) nanoparticle dispersions previously used for the preparation of aerogel monoliths, here we additionally prepared stable colloidal dispersions of zirconia (ZrO_2) and indium oxide (In_2O_3) nanoparticles using two newly developed synthetic procedures. Despite the high concentrations (>240 mg mL^{-1}) all three dispersions are characterized by a high optical transparency, indicating minimal agglomeration of the nanoparticles (Fig. 1).

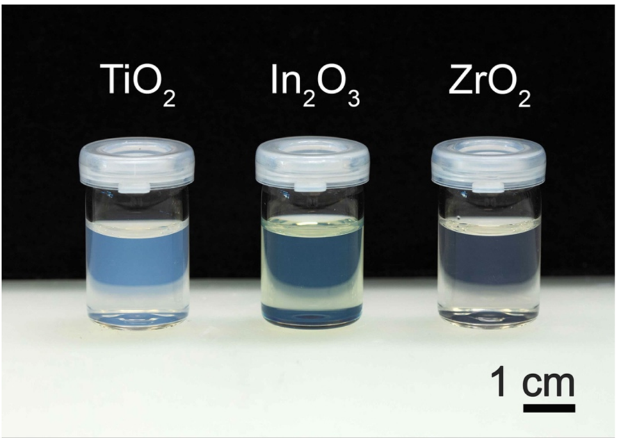

Fig. 1 Digital photograph of concentrated, colloidally stable aqueous dispersions of TiO_2, In_2O_3, and ZrO_2 used in the preparation of nanoparticle-based aerogels with various shapes.

Upon controlled destabilization, the nanoparticles first assemble into larger clusters, which eventually interconnect into a space-spanning network. The resulting gel can be supercritically dried after solvent exchange to fabricate aerogels. In the preparation of nanoparticle-based metal oxide gels, a two-step destabilization process has been proven to be particularly reliable. In this method, gelation is initiated by the addition of a nonsolvent (*e.g.*, acetone), which can be followed up by an increase in temperature, which further destabilizes the dispersion.[39] This combination of triggers allows for precise control over the gelation process and facilitates the production of homogeneous, centimeter-sized aerogel monoliths. The ability to control gelation is fundamental to this study, as it enables the variation of aerogel geometries across a wide range, from conventional centimeter-sized monoliths to millimeter-sized worm-shaped and spherical granules.

Starting with the preparation of conventional monoliths, the nanoparticle dispersions were destabilized using a nonsolvent, followed by gelation at elevated temperatures in cut-open syringes. After gelation, the monoliths were transferred from the syringe molds into a solvent bath. For the preparation of granules, the destabilized dispersion was gelled in an unmodified syringe for a shorter time. This pre-gelled dispersion was then extruded through a nozzle into a solvent bath to form worm-shaped granules. Rapid reformation of the gel network was crucial to prevent the extruded gels from sticking together or even softening and dissolving. To achieve this, the nonsolvent fraction in the solvent baths was increased compared to the pre-gelled dispersions within the syringes. Lastly, spherical granules were produced by adding the pre-gelled dispersion dropwise to an oil layer on top of a solvent bath. To ensure rapid gelation of the spherical droplets within the oil layer, the solvent bath (including the oil layer) was heated to 55 °C. An overview of these processes is given in Fig. 2. In this study we established the processing parameters (nanoparticle concentrations, nonsolvent fractions and temperatures) that made it possible to produce transparent and well-defined aerogels of three different materials and with various shapes, ranging from cylindrical and disc-shaped monoliths to worm-shaped and spherical granules.

Fig. 3–5 display digital photographs of the final aerogels composed of titania (Fig. 3), zirconia (Fig. 4) and indium oxide (Fig. 5). Independent of shape and composition, all aerogels exhibit translucency. The size of the monoliths can reach the centimeter scale, determined from the dimensions of the syringe molds used during preparation.

Optical microscopy reveals that the worm-shaped granules have a relatively uniform diameter of approximately 0.7 mm, while their lengths vary between 2 and 5 mm. Tests with different nozzles (0.2–1.5 mm) showed that the granule diameter can be easily varied through the nozzle diameter. However, the length of the extruded strands was not directly controlled and instead resulted from inadvertent fragmentation during processing. The length of these fragments is directly related to the mechanical stability of the extruded gel. Additional experiments with more concentrated dispersions yielded significantly longer fragments (data not shown). The relatively short fragments of In_2O_3 granules can be explained by the low mechanical

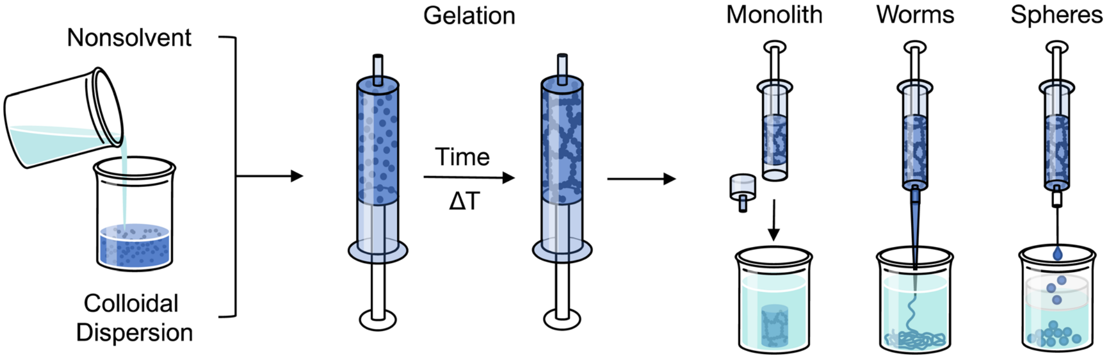

Fig. 2 Process for the preparation of aerogels with different geometries starting from colloidally stable dispersions of nanoparticles. The stability of the dispersion is first reduced with a nonsolvent, then filled into a mold and gelled under heating. Depending on the degree of gelation, the material can be demolded as a monolith, extruded through a nozzle into a solvent bath to form worm-shaped granules, or added dropwise into a solvent bath covered with a silicone oil layer to form spherical granules.

stability of In_2O_3 gels relative to TiO_2 and ZrO_2 gels. We attribute this fact to the larger crystal size of the In_2O_3 nanoparticles (as confirmed by XRD analysis), which leads to fewer cross-links in the gel network and, consequently, weaker gel structures. The spherical granules exhibit a uniform diameter of about 1.3 mm for both TiO_2 and ZrO_2 and ∼1.6 mm for In_2O_3. The sphere

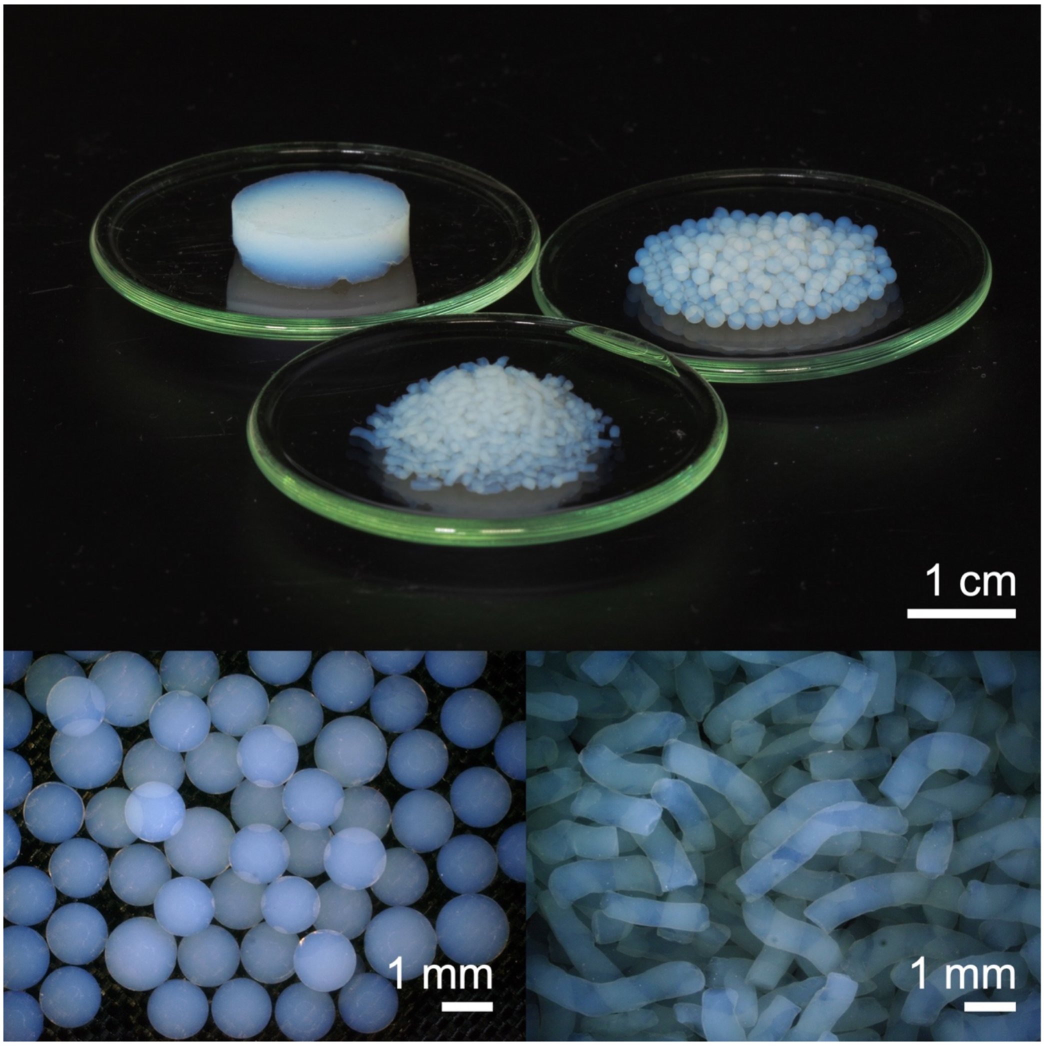

Fig. 3 (Top) The digital image of a TiO_2 nanoparticle-based aerogel monolith in addition to the worm-shaped and spherical aerogel granules. (Bottom) Optical microscopy images of spherical and worm-shaped granules.

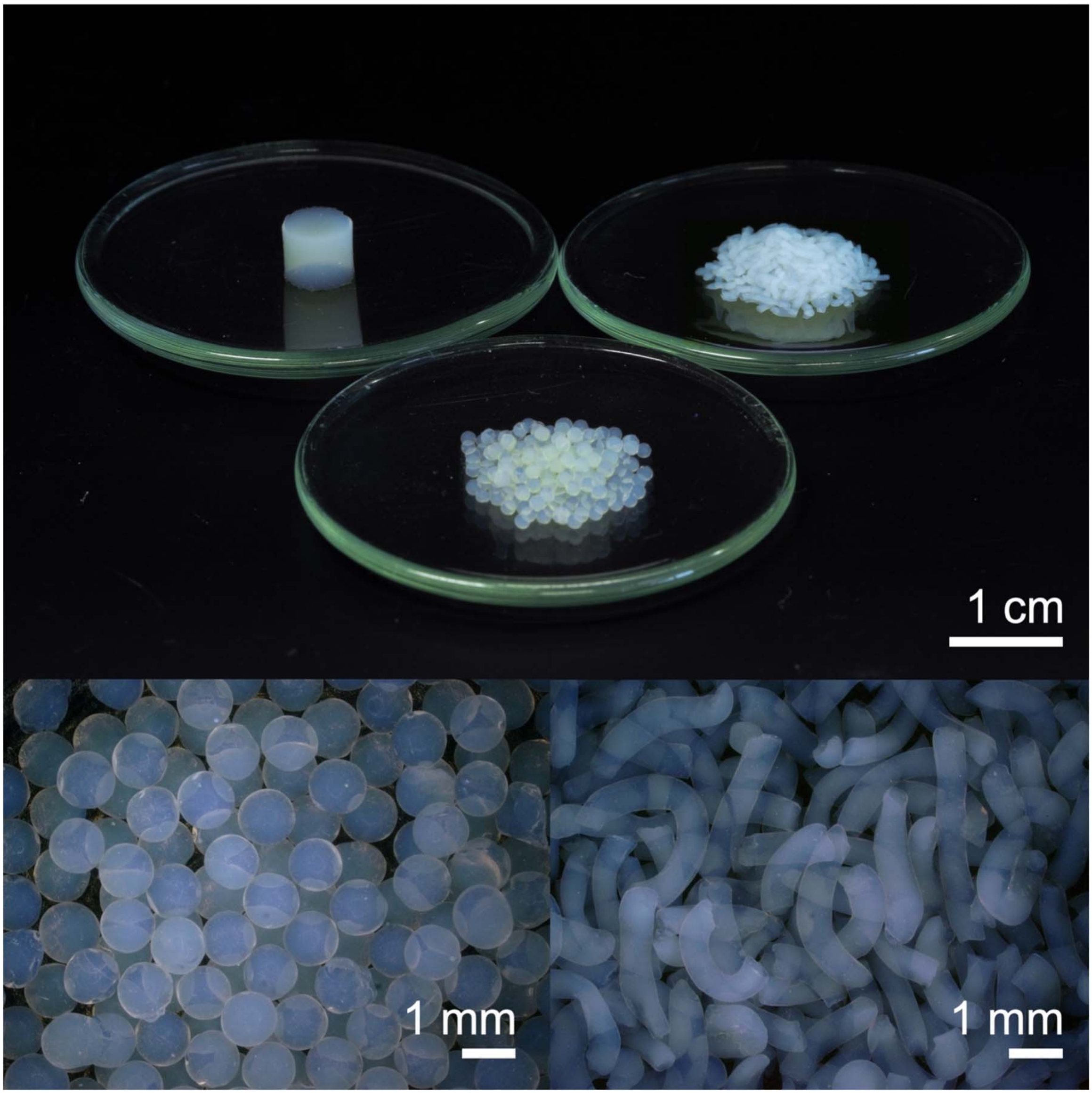

Fig. 4 (Top) The digital image of a ZrO_2 nanoparticle-based aerogel monolith in addition to the worm-shaped and spherical aerogel granules. (Bottom) Optical microscopy images of spherical and worm-shaped granules.

diameter depends on the droplet size and can easily be tuned (*e.g.*, *via* the needle diameter and pre-gelling duration) for a specific application. Moreover, these granules are produced directly without additional processing steps or additives, which are otherwise often required in the production of industrial catalysts.[40]

The process for producing transparent monoliths from metal oxide nanoparticles has previously been demonstrated for TiO_2, and in this study, we extend that approach to ZrO_2 and In_2O_3 nanocrystals, showing that similar translucent monoliths can be fabricated from their colloidal dispersions. Both the fabrication of monoliths and the novel approach for producing aerogel granules require careful optimization of the process parameters to achieve well-defined shapes. The investigation into the gelation behavior of different metal oxide colloids identified two critical factors for forming granules: the degree of gelation before extrusion and the composition of the solvent bath.

The degree of gelation significantly affects the viscoelastic properties of the gel, with thixotropic behavior observed in the early stages, shortly after the transition from a liquid dispersion to a self-supporting gel. This temporary liquefaction under mechanical stress is crucial for extrusion, while rapid regelation after exiting the nozzle ensures that the granules retain their shape and prevents the granules from sticking together. If extrusion occurs too early, the gels tend to flow excessively or stick together. Conversely, extruding at a more advanced stage of gelation, where thixotropy is lost, leads to tearing of the gel, resulting in granules with irregular shapes, poor translucency, and low mechanical strength. According to several studies, the gelation of colloidal dispersions likely progresses through the formation of secondary clusters, which then interconnect into

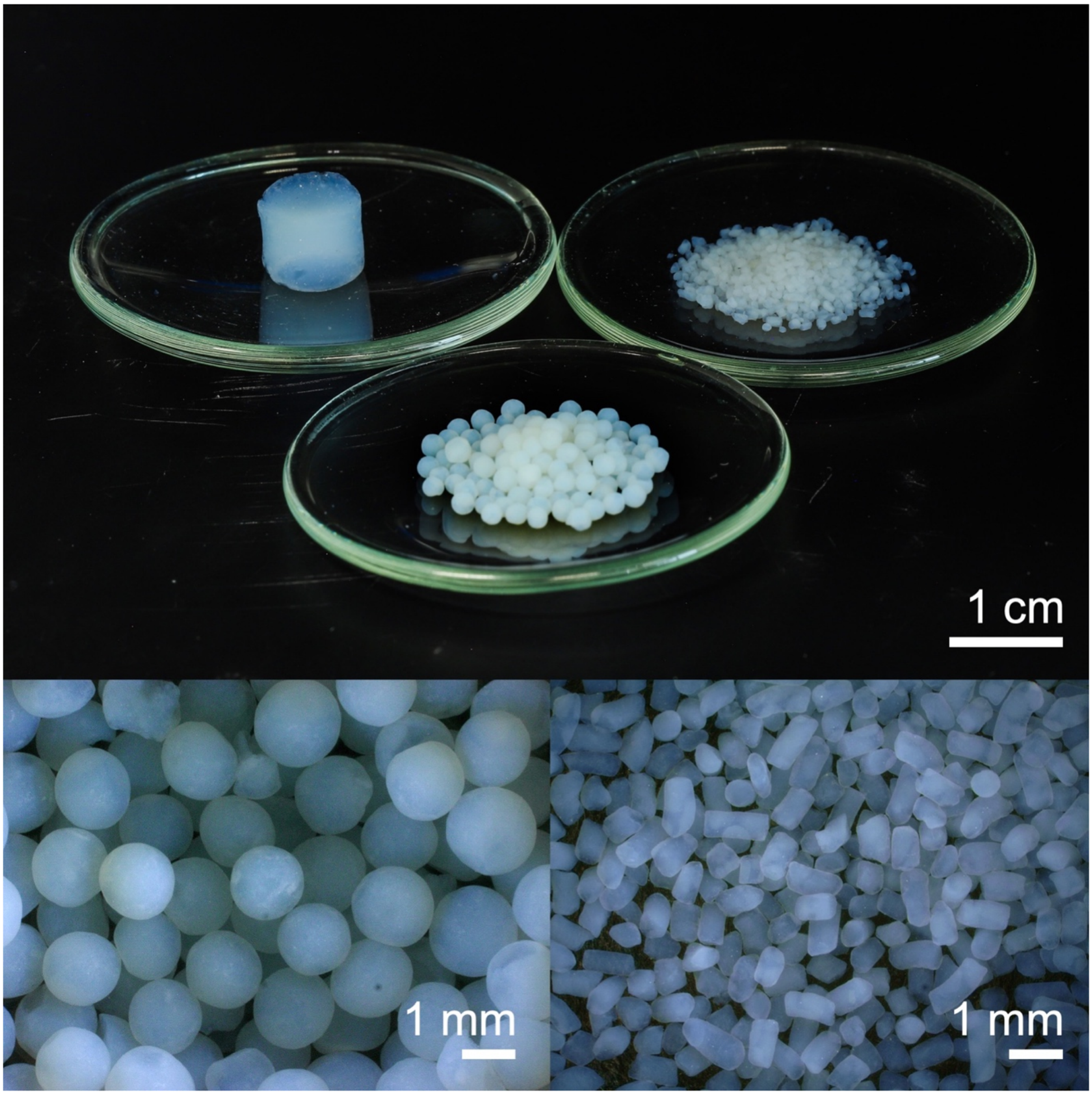

Fig. 5 (Top) The digital image of an In_2O_3 nanoparticle-based aerogel monolith in addition to the worm-shaped and spherical aerogel granules. (Bottom) Optical microscopy images of spherical and worm-shaped granules.

a volume-filling network over time.[9,41–46] We hypothesize that the optimal time for extrusion is when cluster formation and growth are nearly complete, but before the clusters permanently interconnect with each other into a rigid, volume-filling network. At shorter gelation times, the cluster size and number may be too small for a rapid reformation of a self-supporting structure, while with longer gelation times, the network becomes too rigid to be liquefied during extrusion. Therefore, to ensure high-quality granules, it is crucial to precisely control the gelation rate to achieve the desired viscoelastic properties of the gel. This rate can be finely tuned by adjusting the amount of nonsolvent added to the aqueous dispersion or by changing the gelation temperature. Decreasing the amount of nonsolvent or lowering the temperature results in slower gelation, providing more time for any further processing steps.[39]

The composition and temperature of the solvent bath were identified as equally important factors for producing high-quality granules. The solvent bath serves to enhance the gelation rate after extrusion by further decreasing the repulsion between the secondary clusters. This adjustment can be achieved through various methods.[39,47] For the formation of spherical granules, both the solvent bath and the oil layer were preheated to 55 °C to promote faster gelation of the spherical droplets within the oil layer before they enter the solvent phase. Incomplete gelation caused the spherical droplets to deform or break up during their transition from the oil into the solvent layer. For worm-shaped granules, extrusion occurred at room temperature. In both cases, the solvent baths had a higher concentration of nonsolvent compared to the destabilized dispersions. Experiments with different bath compositions revealed that alternatives such as salt solutions (*e.g.*, NaCl and

$CaCl_2$) or alkaline solutions could also be used instead of a nonsolvent/water mixture, providing a variety of processing options (data not shown). Regardless of the destabilizer used, excessive water content in the solvent baths led to the merging, swelling, or dissolution of the extruded gels, while high concentrations of nonsolvents, bases, or salts caused significant shrinkage, increased opacity, or cracking. Therefore, precise control of bath parameters, such as temperature, nonsolvent fraction, ionic strength, and pH, is crucial for achieving translucent, well-defined granules.

By carefully adjusting both gelation conditions and bath composition, TiO_2, ZrO_2, In_2O_3, and potentially various other metal oxide nanoparticles can be effectively converted into porous, transparent aerogel granules. In addition to its versatility, the extrusion process is also scalable and allows the production of worm-shaped aerogel granules on a gram scale. In contrast to the aerogels based on TiO_2 nanoparticles, which have already been intensively investigated in our group,[9,14,15,18,24–26] ZrO_2 and In_2O_3 nanocrystals have not yet been assembled into transparent aerogels. Therefore, the following section provides a detailed structural and morphological characterization of the synthesized nanoparticles and the resulting aerogels by X-ray diffraction, gas sorption measurements, scanning electron microscopy, and thermal gravimetry.

To study the crystal phase purity and crystallite size of the nanoparticles and to investigate possible alterations of these building blocks during processing, we performed powder X-ray diffraction (XRD) on the dried dispersions and the powdered aerogels (Fig. 6). All samples exhibit excellent crystallinity with an identical crystallite size and crystal structure for the respective material, indicating that the original nanocrystalline building blocks remain unaltered during the gelation and drying processes. The crystallite sizes were estimated using the Scherrer equation to be approximately 3.1 nm for TiO_2 (101 reflection), 2.9 nm for ZrO_2 (220 reflection), and 6.8 nm for In_2O_3 (222 reflection). The XRD pattern for TiO_2 corresponds to the anatase phase, consistent with previous studies.[48,49] For ZrO_2, the pattern corresponds to the tetragonal or cubic phase, respectively, with no distinct peaks from the monoclinic phase. This is consistent with similar syntheses showing that ZrO_2 nanocrystals around 3 nm in size tend to crystallize in the metastable tetragonal phase, whereas larger particles (above 8 nm) typically adopt the room-temperature stable monoclinic phase.[50,51] However, the broad diffraction peaks, characteristic of nanocrystalline materials, make it challenging to distinguish between the tetragonal and cubic phases of ZrO_2 due to their similar lattice constants. According to microscopy studies and first principles computer simulations,[52] the phase transition from the tetragonal to the cubic phase occurs if particle sizes become smaller than 2.1 nm. Given a crystallite size of 2.9 nm, we thus assume that the crystal structure of the as-synthesized ZrO_2 nanoparticles is tetragonal. For In_2O_3, the XRD pattern closely matches that of the cubic phase, which is consistent with a previous report on nanocrystalline In_2O_3 synthesized *via* a similar method.[53]

In the production of aerogel granules, the gel network is disrupted and rearranged during extrusion, which raises the question of whether this process influences the microstructural properties of the aerogel granules compared to the monoliths. We therefore conducted gas sorption measurements to investigate the surface areas and pore size distributions of the three geometries (Fig. 7). The obtained surface areas vary only slightly with shape, with no clear trend between the different geometries. All aerogels feature high surface areas of 500–550 m^2 g^{-1} (TiO_2), 330–390 m^2 g^{-1} (ZrO_2) and 110–130 m^2 g^{-1} (In_2O_3). These values are close to the theoretical surface areas calculated from the crystallite size and crystal bulk density of the individual nanoparticles (TiO_2: 500 m^2 g^{-1}, ZrO_2: 340 m^2 g^{-1}, and In_2O_3: 125 m^2 g^{-1}). This finding indicates that the network structures of all aerogels are very finely branched and readily accessible to gases. The pore size distribution for TiO_2 aerogels, centered at around 35 nm, is consistent across all shapes and aligns well with previous studies.[14,18,26] In contrast, ZrO_2 aerogels show variability in pore sizes: worm-shaped granules exhibit the largest pores, approximately 75 nm, monoliths have intermediate pore sizes around 40 nm, and spheres display the smallest pore sizes, around 25 nm. We attribute these differences to the varying degrees of macroscopic shrinkage of the gels observed during solvent exchange. Worm-shaped granules, which were destabilized and extruded in acetone, experienced minimal shrinkage due to the absence of strong solvent gradients. Conversely, monoliths and spheres, destabilized with

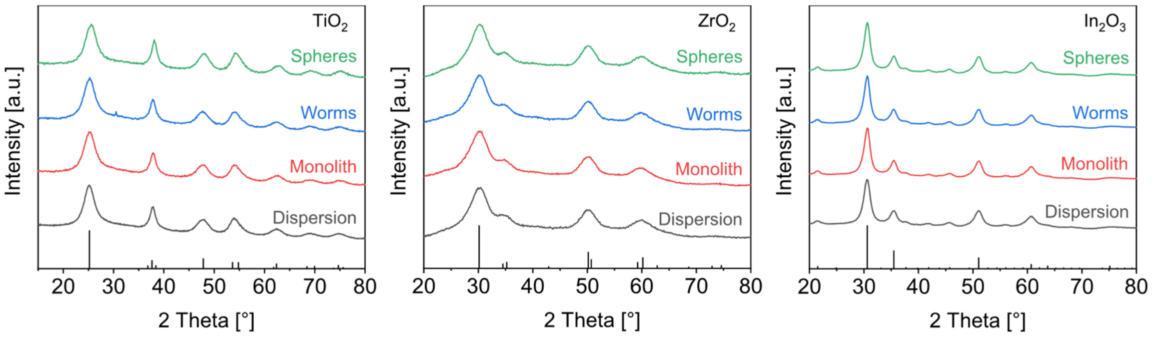

Fig. 6 XRD patterns of the dried TiO_2, In_2O_3, and ZrO_2 dispersions compared with the patterns obtained for ground aerogels of different shapes. The phase and crystallite size of the initial building blocks are fully preserved after assembly and drying. Reference patterns: anatase TiO_2 (ICSD: 193269), tetragonal-ZrO_2 (ICSD: 85322), and cubic-In_2O_3 (ICSD: 14387).

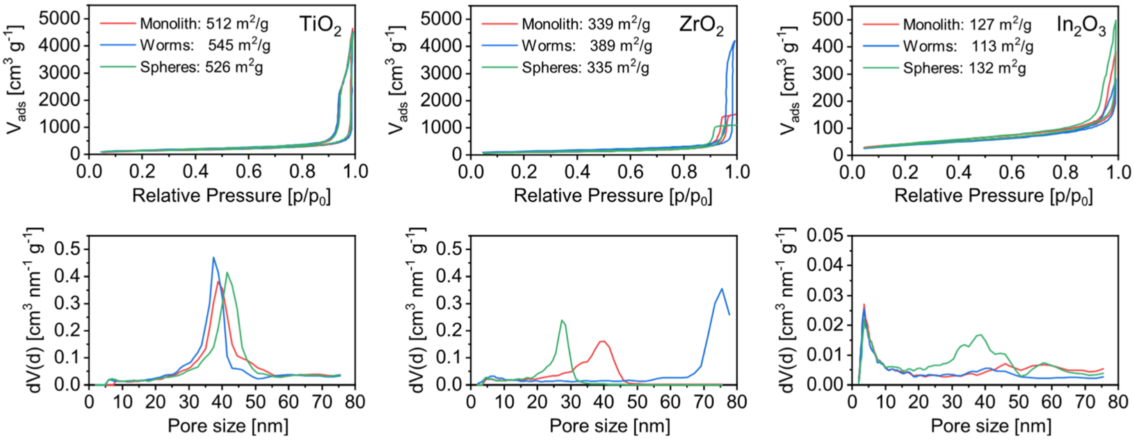

Fig. 7 Nitrogen sorption isotherms and surface area (Top) and pore size distribution (Bottom) of TiO_2, ZrO_2, and In_2O_3 aerogels with different geometries. Note that the scaling of the *y*-axis for In_2O_3 has been adjusted for better readability.

dioxane and subjected to a more rapid solvent exchange with acetone, showed greater shrinkage. Measurements of the dimensions and weight revealed a density of about 300 g cm^{-3} for the monolith and 500 g cm^{-3} for the spheres, which is consistent with the observed shift in mean pore size from 40 nm to 25 nm. For In_2O_3, the pore size appears to exceed 80 nm, placing it outside the detection range of gas sorption analysis, as reflected by the flat isotherm and the small, detected pore volume. These characteristics are likely due to the larger crystallite size of In_2O_3 (~7 nm) compared to TiO_2 and ZrO_2 (~3 nm). In aerogels with similar porosity (*i.e.*, a similar volume fraction of the solid), larger particles lead to a network with thicker branches and thus larger void spaces.

Scanning electron micrographs (Fig. 8) reveal a finely branched structure for all three oxides, with no significant differences observed between the various aerogel shapes. In the case of TiO_2, the building blocks appear slightly more fused, showing rod-like sections that can be attributed to the oriented attachment of the Trizma-functionalized TiO_2 nanoparticles.[48,54] For ZrO_2 and In_2O_3, the individual building blocks are more distinct. In all three systems, the branch diameter ranges between 10 and 20 nm, which is significantly larger than the crystallite size estimated by XRD. This discrepancy is most likely due to the coarsening of microstructural features during the sputter coating process required for imaging[55] rather than the agglomeration of primary particles during gelation. Such a high degree of agglomeration would typically result in much lower surface areas or a higher degree of microporosity, neither of which were observed during gas sorption analysis.

Dioxane was used as the destabilizer to initiate gelation and as nonsolvent in the solvent baths in the production of the spherical aerogels. Unlike most other water-miscible, low-polarity organic solvents, dioxane has a higher density than silicone oil, which is necessary to maintain a floating oil layer on the solvent bath, allowing the droplets to adapt a spherical shape before they gel. However, aqueous dioxane solutions are partially miscible with silicone oil, raising concerns about possible silicone contamination in the final aerogels. To investigate this, thermogravimetric analysis (TGA) was performed on all aerogel shapes to compare and assess potential silicone residues. As shown in Fig. 9, the mass loss profiles across the three geometries are very similar, indicating that the spherical samples do not suffer from significant oil contamination. Among the materials, TiO_2 shows the highest total mass loss (~21%), followed by ZrO_2 (~17%) and In_2O_3 (~7%). This trend is expected as the amount of surface adsorbates scales with the surface area, decreasing from TiO_2 (~530 m^2 g^{-1}) to ZrO_2 (~350 m^2 g^{-1}) and In_2O_3 (~120 m^2 g^{-1}).

The TGA profile and differential scanning calorimetry (DSC) curve for In_2O_3 differ notably from those of TiO_2 and ZrO_2. We attribute this variation to the different precursors used during synthesis – an acetate precursor for In_2O_3 and chloride precursors for TiO_2 and ZrO_2 – resulting in different synthesis by-products and surface adsorbed species.[56] The endothermic mass losses observed at around 100 °C for all three materials are ascribed to the evaporation of surface adsorbed water and residual low boiling-point solvents, such as acetone and 1,4-dioxane. TiO_2 and ZrO_2 exhibit a broad exothermic peak in DSC at around 280 °C, which we attribute to the decomposition of surface-bound benzyl alcohol and Trizma (for TiO_2). Both samples show a less pronounced peak at around 450–500 °C, which can be explained by the decomposition of synthesis by-products, such as benzyl ether and benzoic acid.[57,58] The DSC curve for In_2O_3 reveals a sharp peak at around 305 °C, likely due to the loss of surface-bound acetates or other potential synthesis by-products such as benzyl acetate. In contrast, TiO_2 and ZrO_2 exhibit a broad, gradual mass loss from approximately 200 °C to 500 °C. This is hypothesized to result from three concurrent processes: (1) condensation of surface hydroxyl groups (exothermic) followed by desorption of water (endothermic),[49] (2) sintering of the crystallites (exothermic) under the release of water, and (3) desorption of adsorbed HCl (endothermic). XRF analysis confirmed the presence of 4 to 7 wt% of chloride for these two samples (Table S1†), whereas no chloride was detected in the In_2O_3 samples, consistent with the chloride-free synthesis route. Furthermore, XRD studies and

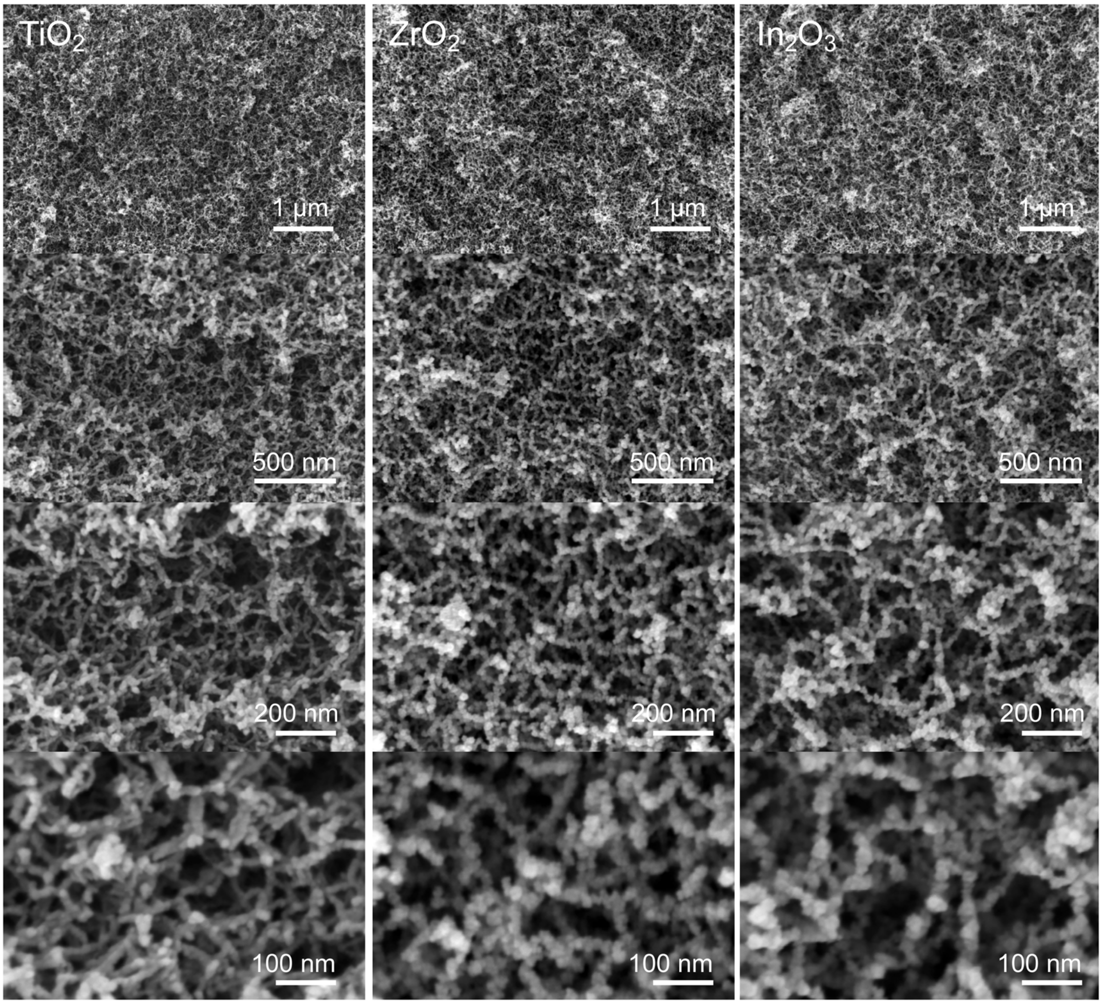

Fig. 8 Representative scanning electron microscopy (SEM) images of worm-shaped TiO_2, ZrO_2, and In_2O_3 aerogel granules at different magnifications. A similar microstructure was found for monolithic aerogels and spherical granules.

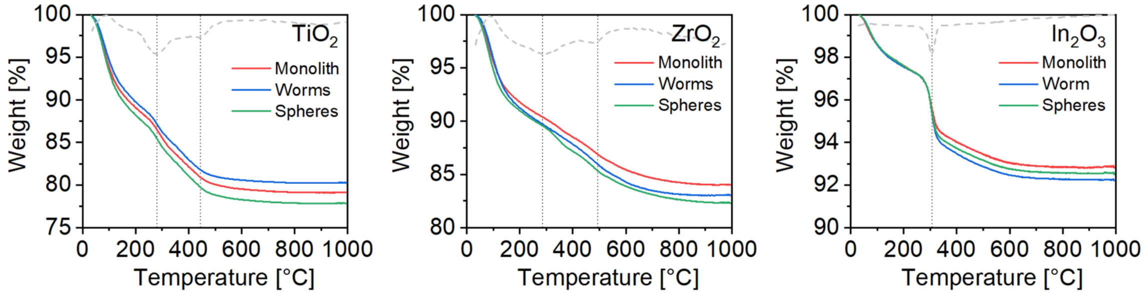

Fig. 9 Thermogravimetric analysis (TGA) of TiO_2, ZrO_2, and In_2O_3 aerogels in different geometries, performed under air flow. The gray line represents the heat flux measured by differential scanning calorimetry (DSC), showing one endothermic peak and two broad exothermic peaks for TiO_2 and ZrO_2, and a single, sharp exothermic peak at around 300 °C for In_2O_3.

gas sorption analysis revealed a gradual growth in crystallite size (from ∼3 nm to ∼10 nm) and loss of surface area (from ∼530 m^2 g^{-1} to ∼150 m^2 g^{-1}) for TiO_2 aerogels annealed at different temperatures between 200 and 500 °C (see Table S3 in the ESI†). In contrast, In_2O_3 aerogels exhibit less sintering, with only slight changes in surface area and crystallite size upon heating to 500 °C. This can be attributed to the larger particle size of In_2O_3 (∼7 nm), which makes it more resistant to sintering compared to the smaller particles of TiO_2 and ZrO_2 (∼3 nm).

As confirmed by XRD, gas sorption analysis and TGA, aerogel granules exhibit almost identical properties to monoliths, showing that the extrusion process does not adversely affect the microstructure of the resulting aerogels. Nevertheless, granules have substantial benefits over monolithic structures. Not only are they much easier to handle than the brittle monoliths, but they also allow for more efficient post-treatment, *e.g.*, to remove organic compounds from the surface, which is often required for (photo-)catalytic applications. Organic residues are preferably removed by UVA, as conventional calcination at elevated temperatures reduces the specific surface area. However, the penetration depth of UVA is very limited for UV-absorbing materials such as TiO_2 and In_2O_3, so the treatment of centimeter-sized aerogels can take several days. In contrast, the granules can be spread in thin layers, allowing much more effective treatment. In addition, the short diffusion paths of granules facilitate solvent exchange and supercritical drying, which drastically reduces fabrication time and cost. As will be shown in the next section, the short diffusion paths also positively affect the mass transport during catalysis.

Photocatalytic measurements

The key motivation for developing aerogels in various shapes was to explore how their geometry affects the photocatalytic performance. These studies were conducted exclusively on TiO_2-based aerogels, as TiO_2 is significantly more photocatalytically active than ZrO_2 and In_2O_3. As a model reaction we studied the oxidation of methanol over worm-shaped and monolithic aerogels with palladium as a cocatalyst (Fig. 10). The Pd/TiO_2 catalysts were characterized by STEM and XRF to verify the distribution and morphology of Pd nanoparticles within the TiO_2 aerogel network. STEM images (Fig. S3–S5†) and XRF data (Table S1†) confirmed the uniform distribution of Pd particles throughout the samples, with a consistent Pd loading of ∼0.17 wt% for both aerogel geometries. Many studies use higher amounts of Pd (≥1 wt%),[59,60] which increases the cost and environmental impact of the catalyst. By using a lower Pd loading, our approach reduces both the economic and environmental footprint while maintaining effective catalytic performance.

The procedure for obtaining the relevant photocatalytic data involved fixing the methanol concentration and total reactant gas flow rate while systematically varying the light intensity (irradiance). Fig. 11a illustrates the methanol conversion rates of monolithic and granular Pd/TiO_2 at varying light intensities (irradiances). For both catalyst geometries, methanol conversion increases linearly with irradiance up to $\sim$200 mW cm^{-2}, after which it plateaus as conversions exceed ∼80%. This linear increase is typical of photocatalytic processes, as the rate is initially limited by the number of available charge carriers, which in turn depends on the number of incident photons. In this reaction-limited regime (irradiance <200 mW cm^{-2}), granules outperform monoliths by 20–50% under equal illumination. We hypothesize that two factors contribute to the lower conversion rate observed in the monolithic aerogels. First, some of the photons are absorbed in the bulk of the monolith, where the supply of reactants from the surface is hindered by the long diffusion paths. Second, the non-uniform flow velocity (faster at the lateral surface and slower at the illuminated circular surface of the monolith) can create depletion zones around the monolithic sample, where the supply of reactants is slower than their consumption. In both cases, the unused charge carriers are lost to recombination rather than driving the desired reaction, which reduces the overall efficiency of the catalytic process. At higher irradiance levels (>400 mW cm^{-2}), the charge carriers become abundant, and the process is mainly constrained by the mass transport rate. In this transport-limited regime, further increases in irradiance lead to only modest gains in conversion. Notably, granules achieve 100% conversion between 400 and 600 mW cm^{-2}, while the monolithic sample does not reach full conversion even at 1000 mW cm^{-2}. This observation highlights the superior mass transport properties of a catalyst bed filled with granules compared to a single aerogel monolith.

The goal in VOC decomposition is the complete oxidation of the organic molecule to CO_2 and water. In the case of methanol, the chemical reaction can be written as follows: $CH_3OH + 3/2\ O_2 \rightarrow CO_2 + 2\ H_2O$. However, methanol (MeOH) can also undergo partial oxidation to formaldehyde (CH_2O): $CH_3OH + 1/2\ O_2 \rightarrow$

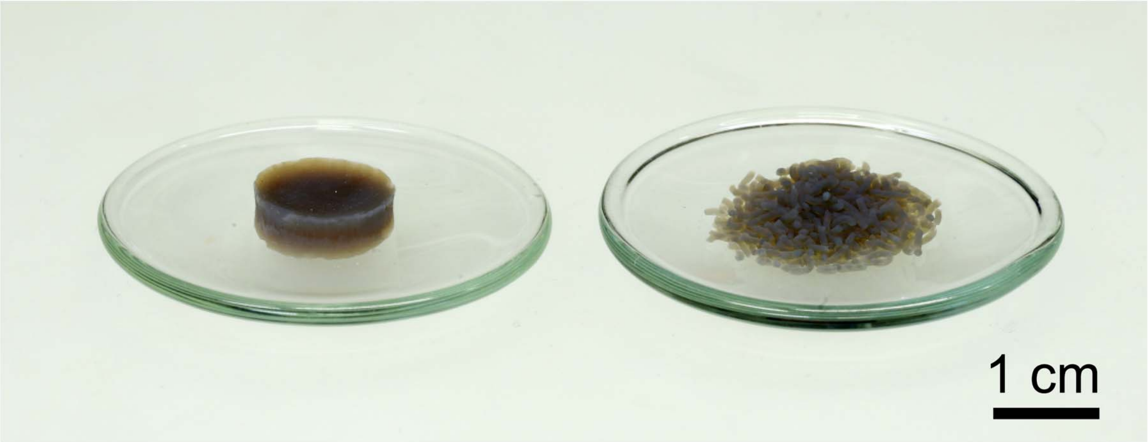

Fig. 10 Digital image of monolithic and worm-shaped Pd/TiO_2 aerogels used for photocatalytic testing. The brown-grey appearance is due to the visible light absorption of the incorporated Pd nanoparticles.

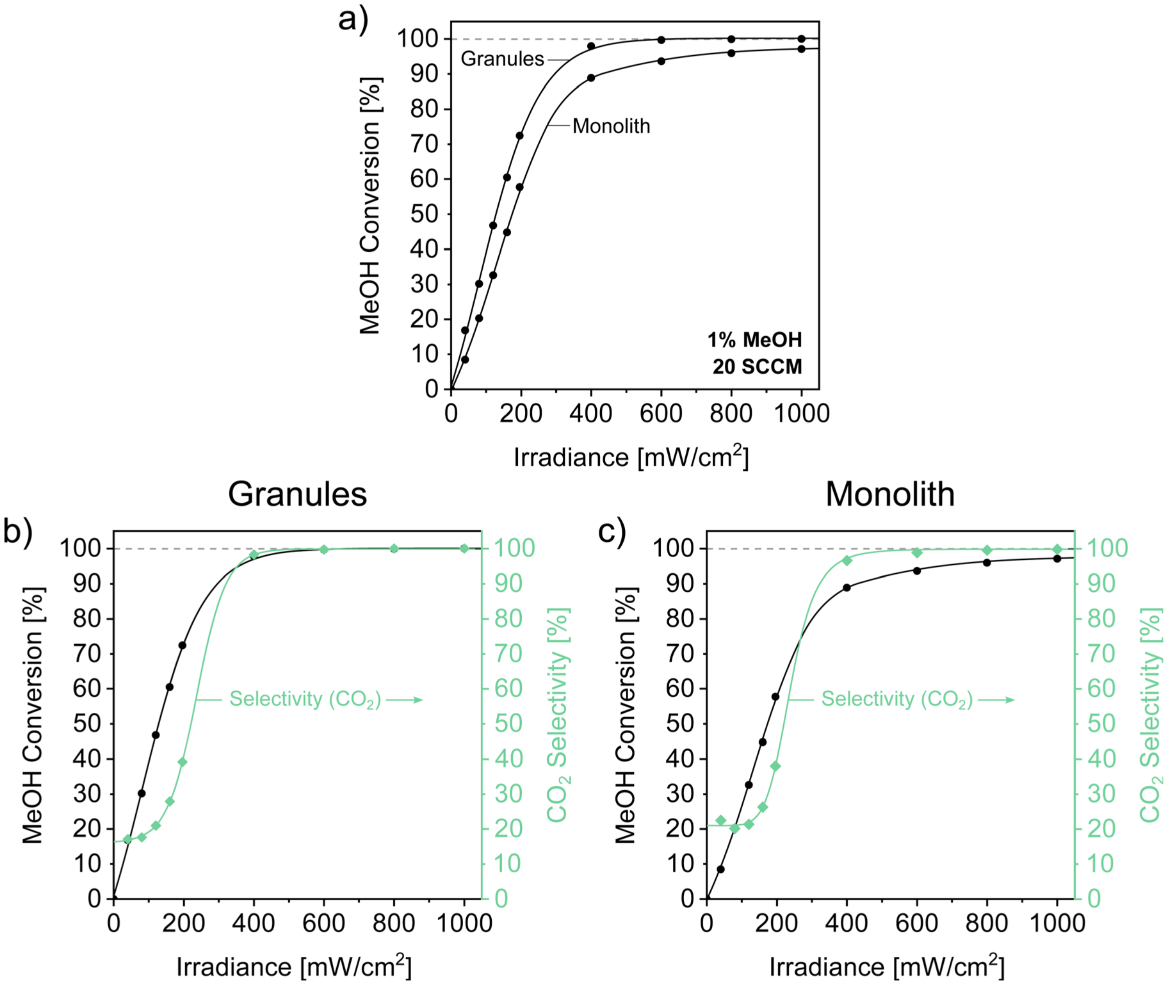

Fig. 11 Photocatalytic methanol conversion of Pd/TiO_2 aerogel monolith *versus* worm-shaped granules at different irradiances. (a) Direct comparison of the methanol conversion of the two geometries. Methanol conversion together with the respective selectivity for CO_2 for (b) the granules and (c) the monolith.

$CH_2O + H_2O$. This reaction is typically undesirable due to the high toxicity of CH_2O. Therefore, the selectivity towards CO_2 (S_{CO_2}) is a critical metric and was analyzed for both monoliths and granules. Fig. 11b and c show the S_{CO_2} for both aerogel geometries, along with the corresponding conversion rates. In addition to the three main products (water, formaldehyde and CO_2), small amounts of a fourth compound were detected, particularly at low irradiances (<200 mW cm^{-2}). We assume that this is methoxymethanol, as identified in previous studies, which forms spontaneously in the co-presence of methanol and formaldehyde.[61] The S_{CO_2} values for both samples remain nearly identical across the entire irradiance range, indicating that selectivity is more dependent on the availability of charge carriers than on mass transport dynamics within the photocatalyst. At low irradiance (<200 mW cm^{-2}), the partial oxidation of methanol (MeOH) to formaldehyde likely results from an insufficient number of charge carriers relative to the available methanol molecules. In this regime, adsorbed MeOH interacts with only a few charge carriers, leading to its conversion to formaldehyde, which desorbs before additional charge carriers become available to complete oxidation to CO_2. At an irradiance above 400 mW cm^{-2}, sufficient charge carriers are available to promote complete oxidation of MeOH to CO_2.

To further elucidate the mass transport differences between the two photocatalyst shapes, the flow rate of the reactant gas (1 mol% methanol in air) was varied. Increasing the flow rate reduces the residence time of the reactants near the catalyst, typically leading to a decrease in conversion. Fig. 12a and b show the irradiance-dependent methanol conversions for both geometries at flow rates between 20 and 75 sccm. As expected, the monolith's performance is significantly more affected by these changes in the flow rate. At an irradiance of 400 mW cm^{-2}, the conversion drops from approximately 90% to 60% for the monolith, whereas granules only show a decrease from about 100% to 80%. At the maximum irradiance (1000 mW cm^{-2}), the granules maintain nearly 100% conversion regardless of the flow rate, while the monolith experiences a 15% reduction in conversion at 75 sccm. As anticipated, the granules show reduced sensitivity to mass transport limitations, allowing for efficient methanol decomposition even at high flow

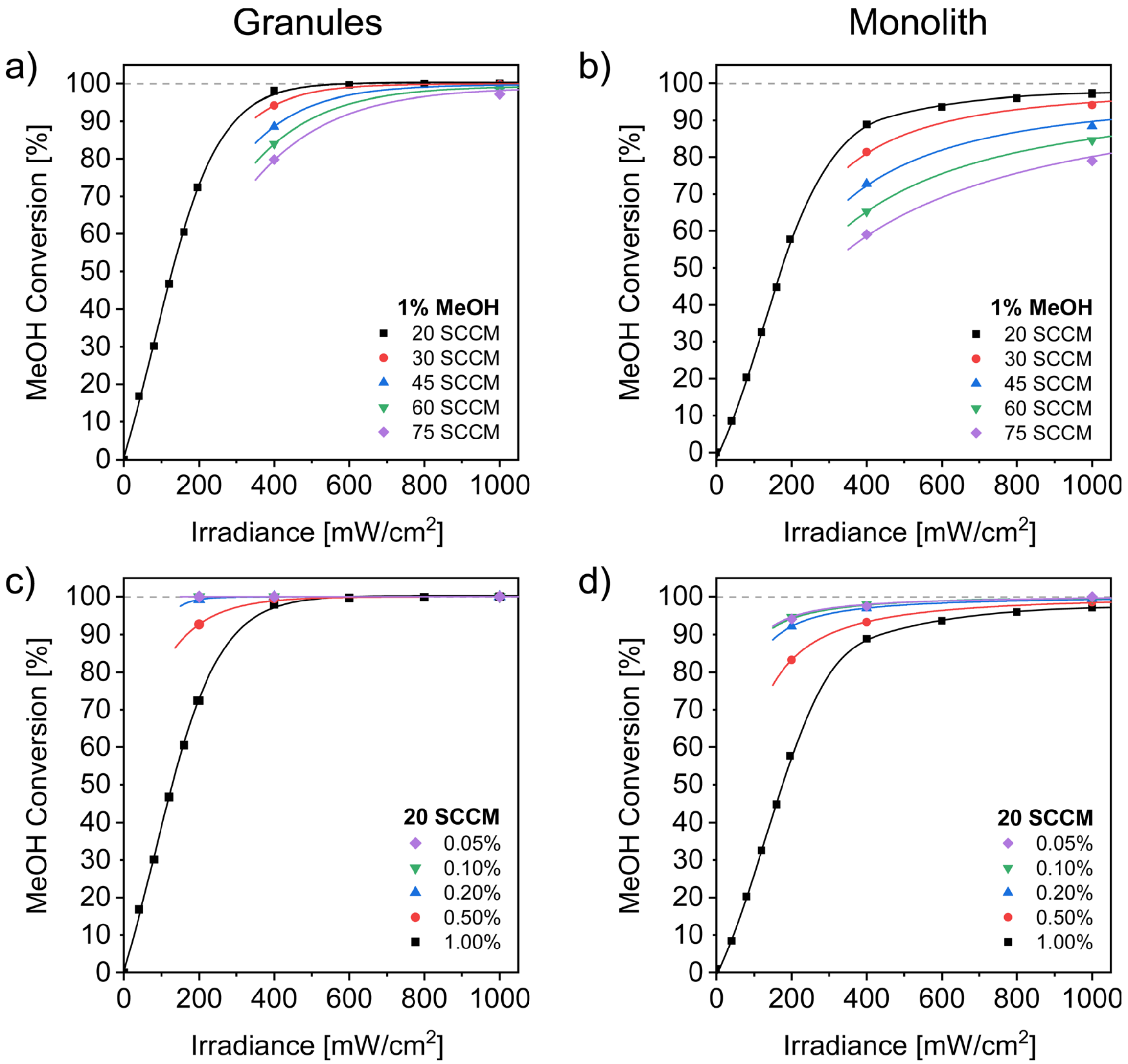

Fig. 12 Photocatalytic performance of Pd/TiO_2 aerogel granules ((a) and (c)) and as monolith ((b) and (d)) at different gas flow rates and methanol concentrations in the gas stream.

rates when exposed to intense irradiance. This finding is critical for maximizing the throughput of a photocatalytic system. However, in addition to the successful degradation of high methanol concentrations (1 mol%) as shown above, there is also a need to study the decomposition of lower VOC concentrations, such as those found in industrial ventilation systems. Typically, the source of VOC emissions, such as the paint drying process in automotive manufacturing, is not directly ventilated; instead, entire sections of warehouses are ventilated, leading to the dilution of VOCs with cleaner air. Catalytic combustion systems must therefore be capable of destroying these trace amounts as well. To simulate such conditions, we conducted experiments using lower methanol concentrations of 500 to 5000 ppm (0.05 to 0.5 mol%), which are more representative of those found in industrial settings and common in the literature.[22,62]

Fig. 12c and d show the irradiance-dependent methanol conversion at concentrations between 0.05 and 1.00 mol% at a constant flow rate of 20 sccm. For both aerogel geometries, the MeOH conversion increases with the dilution of MeOH. At irradiances of 400 mW cm^{-2}, the conversion increases from 89% to 97% for the monolith and from 98% to 100% for the worm-shaped granules. The granules are particularly effective in fully decomposing trace amounts of methanol (500–2000 ppm) even at low irradiances of 200 mW cm^{-2}, whereas in the case of the monolith, significant amounts of methanol (>6%) pass unconverted through the catalyst bed. Both geometries achieve excellent selectivities towards CO_2 (>99.5%) for concentrations below 0.2 mol% methanol (data not shown), even at low irradiances of 200 mW cm^{-2}. This is expected because at very dilute concentrations there is an excess of charge carriers available per molecule of methanol, favoring complete oxidation to CO_2 over partial oxidation to formaldehyde.

Although our previous analysis assumes a purely photocatalytic process driven by charge carrier generation in TiO_2, the UV/vis light absorption of Pd nanoparticles cannot be totally disregarded. It is likely that some UV photons are absorbed by the

Pd nanoparticles, where their energy is converted into heat. The local heating of Pd nanoparticles can potentially drive methanol decomposition *via* a photothermal effect. To investigate this possibility, we conducted additional experiments using visible light (400–800 nm) at 20 sccm and 1% MeOH, which is beyond the absorption edge of TiO_2 and primarily absorbed by the Pd nanoparticles. The results (Fig. S6†) indicate that methanol can indeed be oxidized using visible light only, although the methanol conversion rate does not increase linearly with irradiance as for UV light, but rather exponentially, which is characteristic of a thermally driven process.[63] Under visible light, significant MeOH conversion (>10%) rates are only achieved at irradiances above 200 mW cm^{-2}. These observations suggest that activity at low irradiance UV light (0–200 mW cm^{-2}) is primarily due to photocatalytic rather than thermal effects. By comparing the number of available UV photons to the electrons involved in the reaction, we found that the granules achieve remarkably high apparent quantum efficiencies of 77–85% within this initial linear regime (see the ESI† for details), underscoring the high efficiency of Pd/TiO_2 aerogels in utilizing UV light. Nonetheless, the experiments also show that visible light absorption by the metal phase in metal/semiconductor photocatalysts can play a substantial role in enhancing the reaction rate, especially at higher irradiances. This finding raises the exciting possibility of using broadband illumination, such as solar light (300–2500 nm), rather than relying solely on UV light sources. While significant attention has been given to combining plasmonic nanoparticles, particularly gold, with semiconductors such as TiO_2, our results suggest that non-plasmonic metals such as Pd could also be of significant interest for this purpose.

In summary, we compared the photocatalytic performance of worm-shaped and monolithic Pd/TiO_2 aerogels using methanol oxidation as a model reaction. This system supports both the photocatalytic decomposition of methanol under UV light and photothermal catalysis under visible light, enabling full solar spectrum utilization. Under UV light, two distinct regimes were observed: a reaction-limited regime at low irradiances (0 to 200 mW cm^{-2}), where conversion was constrained by charge carrier availability, and a mass transport-limited regime at higher irradiances (above 400 mW cm^{-2}). The granules consistently outperformed the monoliths under all tested conditions. The improved performance is attributed to larger flow channels between the granules in the catalyst bed, which promote better gas mixing and a more uniform supply of reactants to the catalyst surface. Additionally, the granules' shorter diffusion pathways enable more efficient mass transport into the catalyst. The ability of illuminated (1000 mW cm^{-2}) granules to fully oxidize methanol at a high concentration (1 mol%) and high flow rates (75 sccm, corresponding to a space velocity of ∼115 L g^{-1} h^{-1} or ∼7250 h^{-1}) underscores the potential of nanoparticle-based aerogel photocatalysts for real-world VOC decomposition applications.

4. Conclusions

We presented a new process for producing nanoparticle-based aerogel granules with high optical clarity and high surface area from colloidal dispersions of metal oxide nanocrystals. The process is based on the extrusion of pre-gelled dispersions into a solvent bath at an early stage of gel formation. Depending on the bath setup, both worm-shaped granules and spherical aerogel granules can be produced with high optical clarity and uniform shape on a gram scale. Using this approach, we have successfully prepared aerogel granules from TiO_2, ZrO_2 and In_2O_3 nanocrystals, demonstrating its potential applicability across a wider range of metal oxides. Experiments on the photocatalytic degradation of methanol vapor over TiO_2 aerogels highlight the advantages of extruded granules over traditional monoliths. Worm-shaped granules exhibited significantly enhanced photocatalytic performance, achieving higher conversion rates at elevated flow rates, fully eliminating methanol at concentrations common in industrial applications. This improvement is attributed to the shortened diffusion paths offered by the millimeter-sized granules and the more uniform gas flow through the catalyst bed. In addition to their excellent interaction with gaseous reactants, the granules are more cost-effective to produce and easier to handle, representing a significant step toward the practical implementation of efficient aerogel photocatalysts. Future work will focus on optimizing the granule diameter and Pd content to reduce the required light input, further enhancing system efficiency and practicality. Moreover, the demonstrated photothermal activity under white light suggests that such aerogel catalysts could be adapted for other catalytic reactions, where semiconductor-based photocatalysis has struggled to achieve practical conversion rates thus far, *e.g.*, water splitting, CO_2 reduction, ammonia production, and methane dry reforming.

Data availability

Information supporting the article has been included in the ESI.† Additional data are available on request from the corresponding author.

Conflicts of interest

The authors declare no conflict of interest.

Acknowledgements

We acknowledge ETH Zurich for financial support and the Scientific Center for Optical and Electron Microscopy (ScopeM) for providing access to the electron microscopy facilities. We also thank Till Kyburz and Dr Ana Laura Luna Barron for their support with the design and fabrication of the photoreactor.

References

1 M. R. Hoffmann, S. T. Martin, W. Y. Choi and D. W. Bahnemann, Environmental Applications of Semiconductor Photocatalysis, *Chem. Rev.*, 1995, **95**, 69–96.
2 K. Li, B. S. Peng and T. Y. Peng, Recent Advances in Heterogeneous Photocatalytic CO_2 Conversion to Solar Fuels, *ACS Catal.*, 2016, **6**, 7485–7527.

3 D. Friedmann, A General Overview of Heterogeneous Photocatalysis as a Remediation Technology for Wastewaters Containing Pharmaceutical Compounds, *Water*, 2022, **14**, 3588.

4 M. Zeshan, I. A. Bhatti, M. Mohsin, M. Iqbal, N. Amjed, J. Nisar, N. AlMasoud and T. S. Alomar, Remediation of Pesticides using TiO_2 Based Photocatalytic Strategies: A Review, *Chemosphere*, 2022, **300**, 134525.

5 G. H. Zhou, H. M. Xu, H. Song, J. J. Yi, X. Z. Wang, Z. P. Chen and X. W. Zhu, Photocatalysis Toward Microplastics Conversion: A Critical Review, *ACS Catal.*, 2024, **14**, 8694–8719.

6 C. Xu, P. R. Anusuyadevi, C. Aymonier, R. Luque and S. Marre, Nanostructured Materials for Photocatalysis, *Chem. Soc. Rev.*, 2019, **48**, 3868–3902.

7 A. B. Djurišić, Y. H. Leung and A. M. Ching Ng, Strategies for Improving the Efficiency of Semiconductor Metal Oxide Photocatalysis, *Mater. Horiz.*, 2014, **1**, 400–410.

8 M. Schreck and M. Niederberger, Photocatalytic Gas Phase Reactions, *Chem. Mater.*, 2019, **31**, 597–618.

9 F. Matter and M. Niederberger, Optimization of Mass and Light Transport in Nanoparticle-Based Titania Aerogels, *Chem. Mater.*, 2023, **35**, 7995–8008.

10 F. Matter and M. Niederberger, The Importance of the Macroscopic Geometry in Gas-Phase Photocatalysis, *Adv. Sci.*, 2022, **9**, 2105363.

11 F. Rechberger and M. Niederberger, Synthesis of aerogels: from molecular routes to 3-dimensional nanoparticle assembly, *Nanoscale Horiz.*, 2017, **2**, 6–30.

12 C. Ziegler, A. Wolf, W. Liu, A.-K. Herrmann, N. Gaponik and A. Eychmüller, Modern Inorganic Aerogels, *Angew. Chem., Int. Ed.*, 2017, **56**, 13200–13221.

13 B. Cai, V. Sayevich, N. Gaponik and A. Eychmüller, Emerging Hierarchical Aerogels: Self-Assembly of Metal and Semiconductor Nanocrystals, *Adv. Mater.*, 2018, **30**, 1707518.

14 A. L. Luna, S. Papadopoulos, T. Kyburz, E. Tervoort, L. Novotny and M. Niederberger, Insights into light and mass transport in nanoparticle-based aerogels: the advantages of monolithic 3D photocatalysts, *J. Mater. Chem. A*, 2021, **9**, 22380–22391.

15 M. Schreck, N. Kleger, F. Matter, J. Kwon, E. Tervoort, K. Masania, A. R. Studart and M. Niederberger, 3D Printed Scaffolds for Monolithic Aerogel Photocatalysts with Complex Geometries, *Small*, 2021, **17**, e2104089.

16 M. Castellote and N. Bengtsson, Principles of TiO_2 Photocatalysis, in *Applications of Titanium Dioxide Photocatalysis to Construction Materials: State-of-the-Art Report of the RILEM Technical Committee 194-TDP*, ed. Y. Ohama and D. Van Gemert, Springer, Netherlands: Dordrecht, 2011, pp. 5–10.

17 G. A. Olah, A. Goeppert and G. S. Prakash, *Beyond Oil and Gas: The Methanol Economy*, John Wiley & Sons, 2011.

18 A. L. Luna, F. Matter, M. Schreck, J. Wohlwend, E. Tervoort, C. Colbeau-Justin and M. Niederberger, Monolithic metal-containing TiO_2 aerogels assembled from crystalline pre-formed nanoparticles as efficient photocatalysts for H_2 generation, *Appl. Catal., B*, 2020, **267**, 118660.

19 S. M. Fernandes, B. T. Barrocas, J. V. Nardeli, M. F. Montemor, E. Maçoas, M. C. Oliveira, C. C. C. R. de Carvalho, A. Lauria, M. Niederberger and A. C. Marques, Maximizing photocatalytic efficiency with minimal amount of gold: solar-driven TiO_2 photocatalysis supported by MICROSCAFS® for facile catalyst recovery, *J. Environ. Chem. Eng.*, 2024, **12**, 112043.

20 A. Primo, A. Corma and H. Garcia, Titania supported gold nanoparticles as photocatalyst, *Phys. Chem. Chem. Phys.*, 2011, **13**, 886–910.

21 M. S. Kamal, S. A. Razzak and M. M. Hossain, Catalytic Oxidation of Volatile Organic Compounds (VOCs) – A Review, *Atmos. Environ.*, 2016, **140**, 117–134.

22 Y. Guo, M. Wen, G. Li and T. An, Recent Advances in VOC Elimination by Catalytic Oxidation Technology onto Various Nanoparticles Catalysts: A Critical Review, *Appl. Catal., B*, 2021, **281**, 119447.

23 T. H. Tan, J. Scott, Y. H. Ng, R. A. Taylor, K.-F. Aguey-Zinsou and R. Amal, Understanding Plasmon and Band Gap Photoexcitation Effects on the Thermal-Catalytic Oxidation of Ethanol by TiO_2-Supported Gold, *ACS Catal.*, 2016, **6**, 1870–1879.

24 F. Rechberger and M. Niederberger, Translucent nanoparticle-based aerogel monoliths as 3-dimensional photocatalysts for the selective photoreduction of CO_2 to methanol in a continuous flow reactor, *Mater. Horiz.*, 2017, **4**, 1115–1121.

25 J. Kwon, K. Choi, M. Schreck, T. Liu, E. Tervoort and M. Niederberger, Gas-Phase Nitrogen Doping of Monolithic TiO_2 Nanoparticle-Based Aerogels for Efficient Visible Light-Driven Photocatalytic H_2 Production, *ACS Appl. Mater. Interfaces*, 2021, **13**, 53691–53701.

26 J. Kwon, K. Choi, E. Tervoort and M. Niederberger, One-Pot Microwave Synthesis of Pd Modified Titanium Dioxide Nanocrystals for 3D Aerogel Monoliths with Efficient Visible-Light Photocatalytic Activity in a Heated Gas Flow Reactor, *J. Mater. Chem. A*, 2022, **10**, 18383–18395.

27 M. Rebber, M. Trommler, I. Lokteva, S. Ehteram, A. Schropp, S. König, M. Fröba and D. Koziej, Additive-Free, Gelled Nanoinks as a 3D Printing Toolbox for Hierarchically Structured Bulk Aerogels, *Adv. Funct. Mater.*, 2022, **32**, 2112914.

28 S. T. Sie and R. Krishna, Process Development and Scale Up: II. Catalyst Design Strategy, *Rev. Chem. Eng.*, 1998, **14**, 159–202.

29 L. Thoni, B. Klemmed, M. Georgi, A. Benad, S. Klosz and A. Eychmüller, Continuous droplet reactor for the production of millimeter sized spherical aerogels, *RSC Adv.*, 2020, **10**, 2277–2282.

30 X. Li, G. Qin, Y. Wang and W. Wei, Preparation and Characterization of Equimolar SiO_2–Al_2O_3–TiO_2 Ternary Aerogel Beads, *J. Porous Mater.*, 2014, **21**, 611–621.

31 Y. Yu, M. Zhu and J. Fang, Structure and Thermal Properties of Millimeter-Scale Alumina Aerogel Beads Formed by a Modified Ball Dropping Method, *RSC Adv.*, 2017, **7**, 1540–1545.

32 B. Ohtani, R. M. Bowman, D. P. Colombo, H. Kominami, H. Noguchi and K. Uosaki, Femtosecond Diffuse Reflectance Spectroscopy of Aqueous Titanium (IV) Oxide Suspension: Correlation of Electron-Hole Recombination Kinetics with Photocatalytic Activity, *Chem. Lett.*, 1998, **27**, 579–580.

33 S. Revah and J. M. Morgan-Sagastume, Methods of Odor and VOC Control, in *Biotechnology for Odor and Air Pollution Control*, ed. Z. Shareefdeen and A. Singh, Springer Berlin Heidelberg, Berlin, Heidelberg, 2005, pp. 29–63.

34 F. J. Heiligtag, M. J. I. Airaghi Leccardi, D. Erdem, M. J. Süess and M. Niederberger, Anisotropically Structured Magnetic Aerogel Monoliths, *Nanoscale*, 2014, **6**, 13213–13221.

35 F. Rechberger, E. Tervoort and M. Niederberger, Nonaqueous sol-gel synthesis of $InTaO_4$ nanoparticles and their assembly into macroscopic aerogels, *J. Am. Ceram. Soc.*, 2017, **100**, 4483–4490.

36 M. Horn, C. F. Schwerdtfeger and E. P. Meagher, Refinement of the structure of anatase at several temperatures, *Z. Kristallogr. – Cryst. Mater.*, 1972, **136**, 273–281.

37 V. P. Sirotinkin, L. I. Podzorova, N. A. Mikhailina and O. I. Pen'kova, X-ray Diffraction Study of Structural Changes in High-Strength Ceramics Based on Zirconium Oxide with Additions of Ytterbium and Neodymium Oxides after Hydrothermal Treatment, *Crystallogr. Rep.*, 2022, **67**, 278–285.

38 M. Marezio, Refinement of the crystal structure of In_2O_3 at two wavelengths, *Acta Crystallogr.*, 1966, **20**, 723–728.

39 F. Matter, A. L. Luna and M. Niederberger, From colloidal dispersions to aerogels: how to master nanoparticle gelation, *Nano Today*, 2020, **30**, 100827.

40 B. Kraushaar-Czarnetzki and S. P. Müller, Shaping of Solid Catalysts, in *Synthesis of Solid Catalysts*, ed. K. P. de Jong, John Wiley & Sons, 2009, pp. 173–199.

41 P. Stolzenburg, B. Hämisch, S. Richter, K. Huber and G. Garnweitner, Secondary Particle Formation during the Nonaqueous Synthesis of Metal Oxide Nanocrystals, *Langmuir*, 2018, **34**, 12834–12844.

42 S. Jungblut, J. O. Joswig and A. Eychmüller, Diffusion- and reaction-limited cluster aggregation revisited, *Phys. Chem. Chem. Phys.*, 2019, **21**, 5723–5729.

43 S. Jungblut, J. O. Joswig and A. Eychmüller, Diffusion-Limited Cluster Aggregation: Impact of Rotational Diffusion, *J. Phys. Chem. C*, 2019, **123**, 950–954.

44 P. J. Lu, J. C. Conrad, H. M. Wyss, A. B. Schofield and D. A. Weitz, Fluids of clusters in attractive colloids, *Phys. Rev. Lett.*, 2006, **96**, 028306.

45 L. Korala and S. L. Brock, Aggregation Kinetics of Metal Chalcogenide Nanocrystals: Generation of Transparent CdSe (ZnS) Core (Shell) Gels, *J. Phys. Chem. C*, 2012, **116**, 17110–17117.

46 M. Y. Lin, H. M. Lindsay, D. A. Weitz, R. C. Ball, R. Klein and P. Meakin, Universality in colloid aggregation, *Nature*, 1989, **339**, 360–362.

47 F. Matter, M. Niederberger and F. Putz, Colloidal Nanocrystals: A Toolbox for Materials Chemistry, *Chimia*, 2021, **75**, 387–397.

48 J. Polleux, N. Pinna, M. Antonietti and M. Niederberger, Ligand-Directed Assembly of Preformed Titania Nanocrystals into Highly Anisotropic Nanostructures, *Adv. Mater.*, 2004, **16**, 436–439.

49 T. Kotsokechagia, F. Cellesi, A. Thomas, M. Niederberger and N. Tirelli, Preparation of Ligand-Free TiO_2 (Anatase) Nanoparticles through a Nonaqueous Process and Their Surface Functionalization, *Langmuir*, 2008, **24**, 6988–6997.

50 P. Stolzenburg and G. Garnweitner, Experimental and Numerical Insights into the Formation of Zirconia Nanoparticles: A Population Balance Model for the Nonaqueous Synthesis, *React. Chem. Eng.*, 2017, **2**, 337–348.

51 K. De Keukeleere, J. De Roo, P. Lommens, J. C. Martins, P. Van Der Voort and I. Van Driessche, Fast and Tunable Synthesis of ZrO_2 Nanocrystals: Mechanistic Insights into Precursor Dependence, *Inorg. Chem.*, 2015, **54**, 3469–3476.

52 S. Tsunekawa, S. Ito, Y. Kawazoe and J. T. Wang, Critical Size of the Phase Transition from Cubic to Tetragonal in Pure Zirconia Nanoparticles, *Nano Lett.*, 2003, **3**, 871–875.

53 D. Caruntu, K. Yao, Z. Zhang, T. Austin, W. Zhou and C. J. O'Connor, One-Step Synthesis of Nearly Monodisperse, Variable-Shaped In_2O_3 Nanocrystals in Long Chain Alcohol Solutions, *J. Phys. Chem. C*, 2010, **114**, 4875–4886.

54 J. Polleux, N. Pinna, M. Antonietti, C. Hess, U. Wild, R. Schlogl and M. Niederberger, Ligand Functionality as a Versatile Tool to Control the Assembly Behavior of Preformed Titania Nanocrystals, *Chem.–Eur. J.*, 2005, **11**, 3541–3551.

55 L. Juhász, K. Moldován, P. Gurikov, F. Liebner, I. Fábián, J. Kalmár and C. Cserháti, False Morphology of Aerogels Caused by Gold Coating for SEM Imaging, *Polymers*, 2021, **13**, 588.

56 M. Niederberger and G. Garnweitner, Organic Reaction Pathways in the Nonaqueous Synthesis of Metal Oxide Nanoparticles, *Chem.–Eur. J.*, 2006, **12**, 7282–7302.

57 T. A. Cheema and G. Garnweitner, Phase-controlled synthesis of ZrO_2 nanoparticles for highly transparent dielectric thin films, *CrystEngComm*, 2014, **16**, 3366–3375.

58 A. Pucci, M.-G. Willinger, F. Liu, X. Zeng, V. Rebuttini, G. Clavel, X. Bai, G. Ungar and N. Pinna, One-Step Synthesis and Self-Assembly of Metal Oxide Nanoparticles into 3D Superlattices, *ACS Nano*, 2012, **6**, 4382–4391.

59 S. Xu and D. D. Sun, Significant Improvement of Photocatalytic Hydrogen Generation Rate over TiO_2 with Deposited CuO, *Int. J. Hydrogen Energy*, 2009, **34**, 6096–6104.

60 V. Vaiano, D. Sannino and P. Ciambelli, Steam Reduction of CO_2 on Pd/TiO_2 Catalysts: A Comparison between Thermal and Photocatalytic Reactions, *Photochem. Photobiol. Sci.*, 2015, **14**, 550–555.

61 M. Schreck, *Design Considerations for Aerogels as 3D Gas Phase Photocatalysts*, Doctoral dissertation, ETH Zurich, 2021.

62 R. Liu, H. Wu, J. Shi, X. Xu, D. Zhao, Y. H. Ng, M. Zhang and H. Ding, Recent progress on catalysts for catalytic oxidation of volatile organic compounds: a review, *Catal. Sci. Technol.*, 2022, **12**, 6945–6991.

63 D. Mateo, J. L. Cerrillo, S. Durini and J. Gascon, Fundamentals and applications of photo-thermal catalysis, *Chem. Soc. Rev.*, 2021, **50**, 2173–2210.